

Probing the Rosette Nebula Stellar Bubble with Faraday Rotation

Allison H. Savage, Steven R. Spangler, and Patrick D. Fischer

Department of Physics and Astronomy, University of Iowa, Iowa City, Iowa 52242

ABSTRACT

We report the results of Faraday rotation measurements of 23 background radio sources whose lines of sight pass through or close to the Rosette Nebula. We made linear polarization measurements with the Karl G. Jansky Very Large Array (VLA) at frequencies of 4.4 GHz, 4.9 GHz, and 7.6 GHz. We find the background Galactic contribution to the rotation measure in this part of the sky to be $+147 \text{ rad m}^{-2}$. Sources whose lines of sight pass through the nebula have an excess rotation measure of $50\text{-}750 \text{ rad m}^{-2}$, which we attribute to the plasma shell of the Rosette Nebula. We consider two simple plasma shell models and how they reproduce the magnitude and sign of the rotation measure, and its dependence on distance from the center of the nebula. These two models represent different modes of interaction of the Rosette Nebula star cluster with the surrounding interstellar medium. Both can reproduce the magnitude and spatial extent of the rotation measure enhancement, given plausible free parameters. We contend that the model based on a stellar bubble more closely reproduces the observed dependence of rotation measure on distance from the center of the nebula.

Subject headings: ISM: bubbles, ISM: HII regions, ISM: magnetic fields, plasmas

1. Introduction

Luminous young stars interact with and alter the Interstellar Medium (ISM) from which they form. They interact by photoionizing gas in their vicinity, leading to a propagating ionization front (Spitzer 1968), and by the powerful stellar winds formed by hot, luminous stars. Over the course of a stellar lifetime, stellar winds modify the ISM by inflating a bubble of hot gas surrounding a star cluster. The Weaver et al. (1977) solution for the bubble due to a single star consists of an inner termination shock, a surrounding bubble of hot, low density stellar gas, a contact discontinuity, interstellar medium gas that is photoionized, and finally, an outer shock through which the interstellar gas has passed. A diagram illustrating this structure is given in Figure 1 of Freyer et al. (2003). Within this picture, the visible

HII region corresponds to the annular shell of shocked, photoionized gas. Whether a bubble structure exists, or instead a less dynamic structure corresponding to an ionization front, depends on the mechanical luminosity of the wind or winds in the star cluster. The long term goal of our research program is to better understand how stars in OB associations modify the ISM. In this paper, we present results on Faraday rotation measurements (a diagnostic of plasma properties) on lines of sight through the ionized “bubble” produced by one OB association, and interpret the measurements in the context of models of young clusters.

HII regions are plasmas, and principles of plasma physics determine how these structures evolve and impact the surrounding interstellar medium. One of the most important properties of an astrophysical plasma is the magnetic field. The magnetic field in an HII region or stellar bubble can strongly impact the evolution of the HII region or bubble. At the same time, modification of the magnetic field in the vicinity of an HII region could have consequences for subsequent star formation, properties of interstellar turbulence, and heat flow, among other processes. Measurement of magnetic fields in the interstellar medium is notoriously difficult. One of the best available techniques, and the one utilized in this paper, is Faraday rotation of linearly polarized radio waves from extragalactic radio sources (described in Section 1.1 below; see Minter & Spangler (1996); Haverkorn et al. (2004, 2006); Brown et al. (2003, 2007); Vallee (1993, 2004), among others, for prior uses of this technique). An attractive aspect of Faraday rotation is that it can also be measured for lines of sight that pass through the solar corona, and thus provide information on the coronal magnetic field (Mancuso & Spangler 2000; Ingleby et al. 2007). The fact that the same diagnostic technique can be used in these two media may facilitate comparison between plasma processes in the corona and solar wind, and those in the interstellar medium.

The specific object for study in this paper is the Rosette Nebula, which is a prominent HII region featuring an obvious shell structure and a central cavity (see Figure 1). It is located on the edge of a molecular cloud in the constellation Monoceros. We adopt as its center that of the NGC 2244 star cluster (which is responsible for the Rosette), which is given by Berghöfer & Christian (2002) as RA(J2000)= $06^h 31^m 55^s$, Dec(J2000)= $04^\circ 56' 34''$ ($l=206.5$, $b=-2.1$). The distance to the Rosette is 1600 parsecs and its age is estimated to be 3 ± 1 Myr old (Román-Zúñiga & Lada 2008). Menon (1962) concluded that the Rosette Nebula is an ionization-bounded Strömgren sphere on the basis of radio continuum observations and that its structure is that of an annular shell. This structure is consistent with that of a wind-blown bubble, as mentioned above.

Within the central cavity of the Rosette is the OB stellar association NGC 2244. Photometry and spectroscopy studies put the age of NGC 2244 at less than 4 Myr (Pérez et al. 1989). Evolutionary models place the main-sequence turn off age at 1.9 Myr (Román-Zúñiga & Lada

2008). Despite this age discrepancy, both theoretical models and observations indicate that NGC 2244 is still forming stars (Román-Zúñiga & Lada 2008). There are 21 confirmed pre-main sequence stars, and 113 confirmed stars belonging to NGC 2244, of which at least 7 are O type stars and 24 are B type stars (Román-Zúñiga & Lada 2008; Park & Sung. 2002; Ogura & Ishida. 1981; Wang et al. 2008). The two brightest stars are HD 46223, an O4V star, and HD 46150, an O5V star (Román-Zúñiga & Lada 2008; Wang et al. 2008).

1.1. Faraday Rotation as a Diagnostic Technique for Stellar Bubbles

Faraday rotation is an excellent diagnostic tool for estimating properties of astrophysical plasmas such as the density of the general interstellar medium and the large scale structure of the Galactic magnetic field. Faraday rotation is the rotation in the plane of polarization of a radio wave as it propagates through a plasma that has a magnetic field. The polarization position angle χ of a source, or part of a source, whose radiation has propagated through the ISM is given by

$$\chi = \chi_0 + \left[\left(\frac{e^3}{2\pi m_e^2 c^4} \right) \int_0^L n_e \vec{B} \cdot d\vec{s} \right] \lambda^2 \quad (1)$$

where χ is the polarization position angle, χ_0 is the intrinsic polarization position angle (i.e. that which would be measured in the absence of a medium), e is the fundamental electric charge, m_e is the mass of the electron, c is the speed of light, n_e is the electron density, \vec{B} is the magnetic field, $d\vec{s}$ is the incremental pathlength interval along the line of sight, and λ is the wavelength. The integral in Equation (1) is taken from the source at $s = 0$ to the observer at $s = L$. The variable L represents the effective thickness of the plasma. With this convention, a positive value for the integral corresponds to the average magnetic field pointing from the source to observer, while a negative value represents a mean magnetic field pointing from the observer to the source. The quantity in square brackets is defined as the rotation measure (RM). The fundamental definition of Faraday rotation given in Equation (1) is in cgs units. Values of RM are conventionally given in SI units. This conversion can be accomplished by multiplying the cgs value of the RM by a factor of 10^4 to obtain the SI value. Alternatively, an expression which gives an SI value for the RM given mixed but convenient interstellar units is (Minter & Spangler 1996)

$$RM = 0.81 \int_0^L n_e (cm^{-3}) \vec{B} (\mu G) \cdot d\vec{s} (\text{pc}) \text{ rad m}^{-2} \quad (2)$$

Equation (1) shows that if measurements of $\chi(\lambda)$ are available at two or more wavelengths (preferably three or more), the RM can be measured as the slope of a line through the data

on a plot of χ vs. λ^2 ,

$$RM = \frac{\Delta\chi}{\Delta(\lambda^2)} \quad (3)$$

The wavelengths of observation must be spaced closely enough that there is no possibility of a “wrap” of π radians between two adjacent frequencies of observation. This is referred to as the “ $n\pi$ ambiguity”. A discussion of the constraints on spacing between observing frequencies, as well as an illustration of the difficulties if they are spaced too far apart, is given in Lazio et al. (1990) (see Figures 3 and 4 of that paper). Further details of how we extract RM values from our data are given in Section 3.2.

Among the many studies to have used Faraday rotation in the investigation of interstellar magnetic fields are (Rand and Kulkarni 1989; Minter & Spangler 1996; Brown et al. 2003, 2007; Harvey-Smith et al. 2011; Van Eck et al. 2011). To extract information on the magnetic field, it is necessary to have information on the electron density, since the integrand in Equation (1) is the product of n_e and B_{\parallel} , the parallel component of the interstellar magnetic field. The data sources we use for estimates of n_e are described in detail in Section 4.1 below.

1.2. The Rosette Nebula as a Candidate for Faraday Rotation Measurements

The Rosette Nebula is an excellent object for studies of stellar bubbles via the technique of Faraday rotation. Besides being a prominent HII region with a shell and cavity, the Rosette has other properties which make it an excellent choice for studies of the impact of a young stellar association on the surrounding ISM. The Rosette is in the rough direction of the Galactic anticenter ($l=206.5^\circ$). This gives it a number of advantages relative to HII regions and young star clusters in the inner two quadrants of the Galactic plane. Since star formation regions are relatively rare beyond the solar circle, there is no confusion in the Rosette field with other star formation regions at different distances along the line of sight. By contrast, studies in the Cygnus Region (e.g. Whiting et al. (2009)) are complicated by numerous star formation regions at various distances. Extinction also is less heavy for most anticenter lines of sight. The star cluster responsible for the Rosette Nebula (NGC 2244) is clearly seen, and the spectral types of the stars have been determined.

Another advantage of the Rosette Nebula is its structural simplicity. It resembles the theoretical ideal of a photoionized interstellar bubble as described by the theory of Weaver et al. (1977). Furthermore, the parameters of the bubble structure have been determined by the radio continuum observations of Menon (1962), and later confirmed by Celnik (1983, 1985). Celnik (1985) determined that the Rosette Nebula is a spherical shell of ionized

matter around NGC 2244 on the basis of radio continuum observations at 1.4 GHz and 4.7 GHz with the 100 m telescope at Effelsberg. Celnik also reported values for the inner and outer radius of the shell of gas and the density within the HII region (Celnik 1985)¹. We adopt Celnik’s parameters for the shell density and the structure in our analysis in Section 4.

1.3. Previous results of Faraday Rotation Diagnostics of HII Regions

Whiting et al. (2009) presented a study of the Galactic plane region near the Cygnus OB1 association. The main purpose of Whiting et al. (2009) was to confirm the existence of a “Faraday Rotation Anomaly” in this part of the sky, i.e., a large change in RM over a small distance on the sky. Whiting et al. (2009) argued that this anomaly was due to the plasma bubble associated with the Cygnus OB1 association. Whiting et al. (2009) also developed a simple shell model that reproduced the observed magnitude and the change in RM in Cygnus. In Section 4, we will use this shell model to interpret our data on the Rosette Nebula.

Harvey-Smith et al. (2011) used Faraday rotation and H α measurements with the WHAM spectrograph (Haffner et al. 2003) to measure the electron density and line of sight magnetic fields in several HII regions. Faraday rotation was measured for extragalactic radio sources viewed through the HII regions. They probed 93 lines of sight in 5 HII regions, and found that each HII region displays a coherent magnetic field, with a range of 2 to 6 μ G for the parallel component (Harvey-Smith et al. 2011). Harvey-Smith et al. (2011) briefly compared their RM values with the model presented by Whiting et al. (2009) and concluded that there is no evidence for a shell with an amplified magnetic field in any of the HII regions. Whiting et al. (2009) and Harvey-Smith et al. (2011) thus come to different conclusions about the nature of the plasma shell that comprises an HII region. It should be noted that Whiting et al. (2009) claimed that the Faraday rotation anomaly was consistent with a wind-blown bubble, but did not claim that it was inconsistent with a shell without magnetic field amplification. Additional observations of the sort presented in Whiting et al. (2009) will help resolve this issue. Measurements of RM on a large number of lines of sight through an HII region (in the case of the present paper, the Rosette Nebula) will diagnose the plasma structure of the HII region, and determine if the HII region produces significant modification of the interstellar magnetic field. In time, we plan to carry out such observations on a set of HII regions associated with star clusters of different age, stellar luminosity, and wind power.

¹See Celnik 1985, Section 5.1 for the details of those measurements.

2. Observations

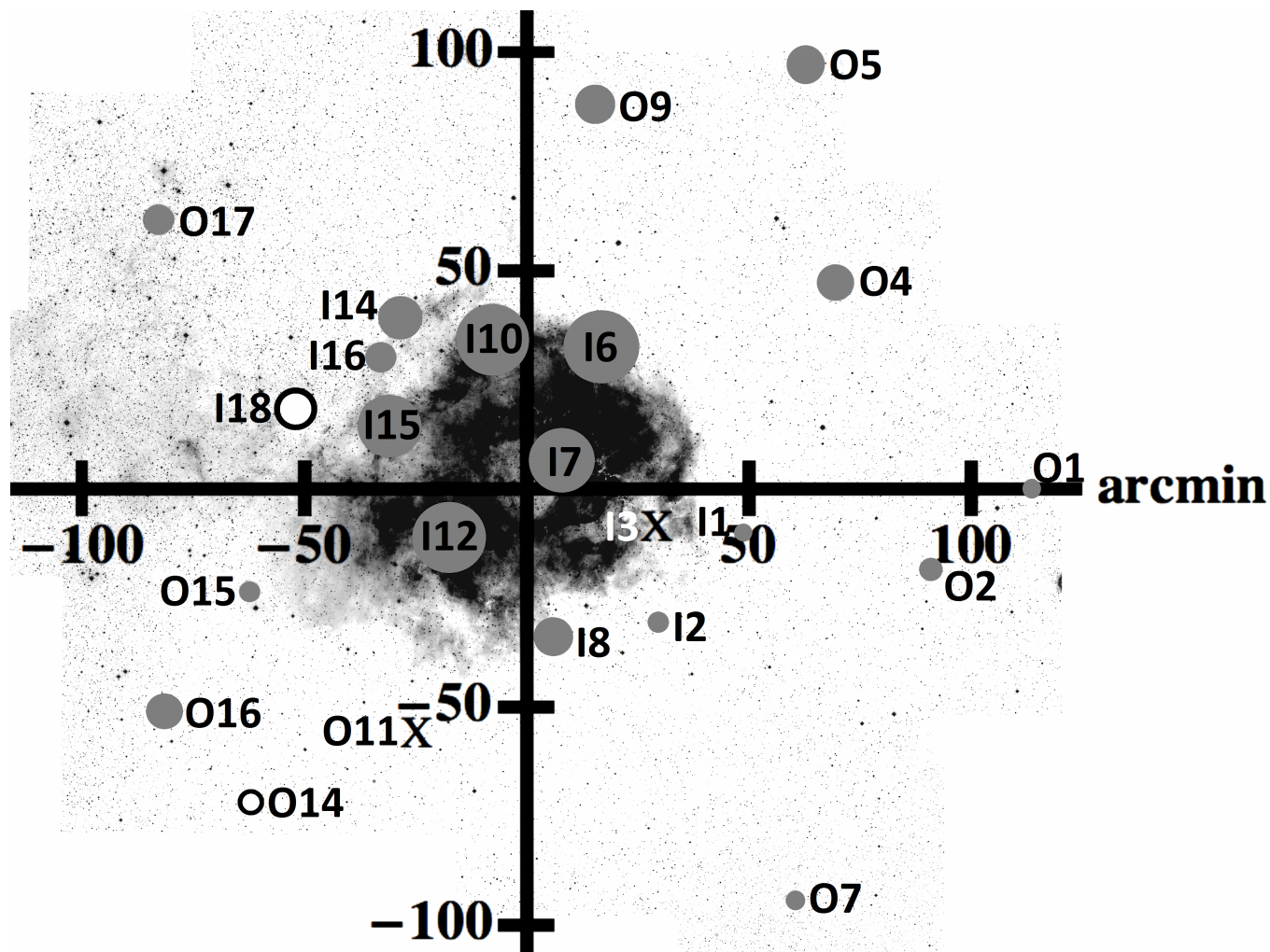


Fig. 1.— A mosaic of the Rosette Nebula compiled from the Palomar Sky Survey II. The interior sources whose lines of sight pass through, or close to, the visible nebula are labeled with the prefix of “I”. The exterior sources whose lines of sight are well outside the visible nebula are labeled with the prefix of “O”. Sources with negative RMs are labeled with open circles and those with positive RMs have solid circles. Depolarized sources are marked with an “X”. The source symbols are scaled with the magnitude of the $\log |RM|$. [The Second Palomar Observatory Sky Survey (POSS-II) was made by the California Institute of Technology with funds from the National Science Foundation, the National Geographic Society, the Sloan Foundation, the Samuel Oschin Foundation, and the Eastman Kodak Corporation. The STScI Digitized Sky Survey can be found at [<http://stdata.stsci.edu/cgi-bin/dssform>.]

All observations were made with the Karl G. Jansky Very Large Array (VLA) radio

telescope of the National Radio Astronomy Observatory during the first several months of commissioning of the upgraded VLA.² Details of the observations and resultant data are given in Table 1. The VLA was in D array for all of the observations. We observed 23 extragalactic radio sources whose lines of sight pass through or close to the Rosette Nebula. The sources were chosen from the NRAO VLA Sky Survey (NVSS), which covers the entire sky north of declination -40° at 1.4 GHz (Condon et al. 1998). We also observed four calibrators, 3C286, J0632+1022, J0643+0857, and 3C138. The calibrator 3C286 is commonly used for absolute calibration of the visibility amplitudes because it has a well known flux density. It is also used to calibrate the origin of the polarization position angle. The source 3C138 was used for independent observations that could also set the flux density scale and determine the origin of the polarization position angle. Specifically, we used our observations of 3C138 to independently confirm the value of the R-L phase difference (used to calibrate the polarization position angle) obtained from 3C286. The source J0632+1022 was the primary calibrator for the project, functioning as the gain calibrator, i.e., determining the complex gain of each antenna as a function of time. This source (J0632+1022) was also used to measure the instrumental polarization, described by the “D factors”, D_R and D_L (Bignell 1982; Sakurai & Spangler 1994). We also observed a second source, J0643+0857, to obtain a completely independent set of D factors which confirmed our instrumental polarization calibration.

In addition to the calibrators, we observed 23 program sources. We had 12 sources whose lines of sight passed through the Rosette Nebula. The remaining 11 sources have lines of sight that pass near the Rosette Nebula but outside the obvious $H\alpha$ -emitting shell. We observed these latter sources so we could establish a background RM value due to the Galactic plane. Figure 1 shows an image of the Rosette Nebula with the positions of our sources superposed.

²The Very Large Array is an instrument of the National Radio Astronomy Observatory. The NRAO is a facility of the National Science Foundation, operated under cooperative agreement with Associated Universities, Inc.

Table 1: Log of Observations

Dates of Observation	March 20, 2010; July 4, 2010; August 22, 2010
Duration of Observing Sessions (h)	5.95; 5.89; 5.94
Frequencies of Observations ^a (MHz)	4136; 4436; 4936; 7636
VLA array	D
Restoring Beam (diameter)	12''8; 19''6 ^b
Number of Scans per Source Per Session	5
RMS Noise Level in Q and U Maps (mJy/Beam)	0.042; 0.048; 0.037 ^c

^aThe observations had 128MHz wide spectral windows centered on the frequencies listed.

^bThe March and July sessions were restored using a beam size of 12''8, and the August session was restored with a 19''6 beam size.

^cAverage RMS noise levels for 4.4 GHz, 4.9 GHz, and 7.6 GHz, respectively.

We observed 128 MHz wide spectral windows centered on three frequencies: 4.436 GHz, 4.936 GHz, and 7.636 GHz. We had three sessions on the VLA (“scheduling blocks”) on March 20, July 4, and August 22, 2010. We also made observations at 4136 MHz for the March and July sources, which would have provided polarization measurements at 4 frequencies. However, we ultimately flagged all 4.1 GHz data due to overwhelming RFI. Table 1 presents a summary of the observations, which includes the date of observation, the duration of the sessions, the frequencies observed, the VLA array, the restoring beam used for each session, the number of scans per source per session, and the characteristic RMS noise level in the Q and U maps. The sources for the March and July sessions were the same, and we observed those sources at all three frequencies. The August session observed additional sources. This new set of sources was observed at 4.4GHz and 4.9GHz only. The intent was to observe these sources at 7.6 GHz as well, but the D array observing season ended before a 4th scheduling block was carried out. Table 2 lists all the sources with a project name in column 1, the RA and Dec (J2000) in columns 2 and 3, respectively, the galactic longitude and latitude in columns 4 and 5, the angular distance between the line of sight and a line of sight passing through the center of the Rosette, ξ , in column 6. The total Clean Flux at 4.9GHz is given in column 7, and in column 8, the number of frequencies observed for each source, where the number 3 corresponds to the set of frequencies of [4.4 GHz, 4.9 GHz, & 7.6 GHz] and the number 2 corresponds to the set [4.4GHz and 4.9GHz]. The range in frequency between 4.4 GHz and 7.6 GHz allows us to obtain RM values that are as low as a few tens of rad m^{-2} , given the errors in the polarization measurements (see Section 3.2 below). The shorter range between 4.4GHz and 4.9GHz allows for measurements of large RM values without being affected by the “ $n\pi$ ambiguity”.

3. Data Reduction

All data reduction was performed with the Common Astronomy Software Applications (CASA) data reduction package. The calibration procedure is similar to that used in our prior Faraday rotation projects with the VLA, such as Whiting et al. (2009) and Minter & Spangler (1996). The procedure for reducing and calibrating the data was as follows.

1. We flagged out measurements corrupted by radio frequency interference (RFI). For all sessions, some antennas were completely flagged because of corrupted or missing data. We also implemented position corrections for a number of antennas. As well as usual systematic flagging procedures (e.g. “Quack”), we visually inspected the data in order to manually remove RFI and other problems.

Table 2: Sources Observed.

Source Name	α (J2000) h m s	δ (J2000) ° ' "	l (°)	b (°)	ξ^a (arcmin)	$S(4.9\text{GHz})^b$ [Jy]	Number of f observed
I1	06 28 39.50	04 47 08.0	206.1	-2.9	49.6	0.017	2
I2	06 29 56.26	04 26 33.0	206.5	-2.7	42.2	0.260	3
I3	06 29 57.30	04 47 45.5	206.2	-2.6	30.6	0.038	3
I6	06 30 50.04	05 29 26.6	205.7	-2.1	36.6	0.013	2
I7	06 31 24.28	05 02 50.8	206.2	-2.1	9.9	0.043	2
I8	06 31 34.31	04 22 34.4	206.8	-2.4	34.4	0.025	3
I10	06 32 31.12	05 30 32.7	205.9	-1.7	35.2	0.024	2
I12	06 33 03.14	04 44 56.0	206.6	-1.9	20.6	0.047	3
I14	06 33 46.34	05 36 54.0	205.9	-1.4	48.9	0.070	3
I15	06 34 00.01	05 10 42.8	206.3	-1.5	34.2	0.021	3
I16	06 34 11.48	05 25 32.0	206.1	-1.3	44.7	0.020	2
I18	06 35 25.96	05 14 15.3	206.4	-1.2	55.4	0.028	2
O1	06 24 18.84	04 57 01.9	205.4	-3.7	113.6	0.150	2
O2	06 25 51.89	04 35 40.2	205.9	-3.6	92.8	0.340	3
O4	06 27 21.09	05 45 37.8	205.1	-2.7	84.0	0.090	3
O5	06 27 36.73	06 32 52.1	204.4	-2.3	115.7	0.066	3
O7	06 27 38.32	03 24 59.6	207.2	-3.7	111.7	0.220	2
O9	06 30 52.53	06 24 50.5	204.9	-1.6	89.6	0.050	3
O11	06 33 32.77	04 00 06.0	207.3	-2.1	61.5	0.110	2
O14	06 35 51.95	03 42 18.0	207.9	-1.8	94.9	0.029	2
O15	06 36 05.69	04 32 40.5	207.1	-1.3	66.9	0.410	3
O16	06 37 23.05	04 05 44.1	207.7	-1.3	96.3	0.029	3
O17	06 37 36.18	05 55 32.5	206.1	-0.4	103.4	0.038	2

^aAngular distance between the line of sight and a line of sight through the nebula. See Section 4.1.

^bTotal flux at 4.9GHz.

2. Calibration of the array, consisting of determination of the complex gains and instrumental polarization parameters (“D factors”), as well as the right-left phase difference for the entire array, was carried out following the online *EVLA Continuum Tutorial* and supplemented by the handbook for the CASA program.³
3. Polarized images of the sources were made from the calibrated visibility data with the CASA task CLEAN. CLEAN is a task that Fourier transforms the data to form the “dirty map” and “dirty beam”, carries out the CLEAN deconvolution algorithm, and restores the image by convolving the CLEAN components with the restoring beam. We produced CLEANed maps of the Stokes parameters I, Q, U, and V. Different weighting schemes in the (u, v) plane were used in the different sessions. The weighting was set to uniform for the March and July sources, but natural weighting was used for the August sources in order to obtain a better signal to noise ratio for the weaker sources observed in that session. The restoring beam for the March and July sources, across all frequency bands, was 12''.8. For the August sources, the restoring beam was 19''.6. The larger restoring beam in the August 2010 session is due to the use of natural rather than uniform weighting in the (u,v) plane. All maps presented utilized external calibration only. A single iteration of phase-only self calibration did not produce an improved signal-to-noise ratio for our maps.

3.1. Imaging the Sources

Having obtained the maps of the Stokes parameters I, Q, U, and V for each source at each frequency, we generated maps of the linear polarized intensity, L, and the polarization position angle, χ

$$L = \sqrt{Q^2 + U^2} \quad (4)$$

$$\chi = \frac{1}{2} \tan^{-1}\left(\frac{U}{Q}\right) \quad (5)$$

For each source and frequency, we worked with images of I, L, and χ . Examples of the images of two of our sources are shown in Figures 2 and 3. Figure 2 shows the I, L, and χ maps of a point source (to the D array), I15, that was found to have a large RM (633 ± 14 rad m⁻²). Figure 3 shows a source, O2, which is resolved to the D array and possesses structure.

³For further reference on data reduction, see the NRAO EVLA Tutorial “EVLA Continuum Tutorial 3C391”. [<http://casaguides.nrao.edu/index.php?title=EVLAContinuumTutorial3C391>]

3.2. Determination of Rotation Measures

In this section, we describe how we obtained RMs from data of the sort shown in Figures 2 and 3. We first identified a local maximum in the polarized intensity in the 4.4GHz map. We then measured the polarization position angle χ at this location for the 2 or 3 frequencies available for this source. Since the sources from the August scheduling block have only two data points, the RM was calculated from Equation (3). There are also larger errors associated with the sources from the August scheduling block due to having only two data points that are only slightly separated in frequency. There are three data points for the sources from the March and July scheduling blocks and the RM was calculated by plotting the polarization position angle, χ , against λ^2 and fitting a line to this relationship. An example of this is illustrated in Figure 4, for the source I15, and Figure 5 for the source O2. All of our RM values were positive except for I18 and a component of O14. Two of the sources, I3 and O11, were depolarized, so we did not obtain a RM for them.

The source I2 requires additional comments. I2 is an interior source from the March and July scheduling blocks. Usually, this would mean that we had polarization data at three frequencies. However, the 4.4GHz data for I2 were excluded from the calculation of the RM measurement. The 4.4GHz data failed a test for data quality that we applied to our observations, as follows. For each source and frequency, the data from each scan was mapped. As discussed in Section 2 above, each source was typically observed for 5 scans during the 6 hour observing session. These scan maps were made in all polarization parameters as well as the total intensity I . The purpose of this exercise was to make sure that no systematic changes occurred during the observing session, due to incorrect correction for instrumental polarization, or similar effects. Once it was determined that the polarization data were “stationary” during the observing session, and that no drastically flawed data were present, I , Q , and U maps as well as maps of the derived quantities L and χ , were made with all available data. Unlike the other sources for which values of χ were within 1σ of the mean values, the χ time series for I2 showed scan-to-scan variations larger than noise. We examined I2 at 4.9GHz and 7.6 GHz, and determined that inconsistent polarization position angles were not present at the higher frequencies. Since we only used two frequencies in determining the RM value for I2, there is a larger error associated with this source. The degree of linear polarization for I2 was extremely low, 0.1% at 4.4GHz, and we attribute the variations of χ to residual instrumental polarization artifacts, which can appear with low values of the degree of linear polarization (Sakurai & Spangler 1994). We retain I2 as one of the sources in our sample because we believe the data from the two higher frequencies are adequate to determine RM . The RM for I2 is consistent with the values for adjacent sources that we determined from measurements at three frequencies, indicating that $n-\pi$ ambiguities are not a problem.

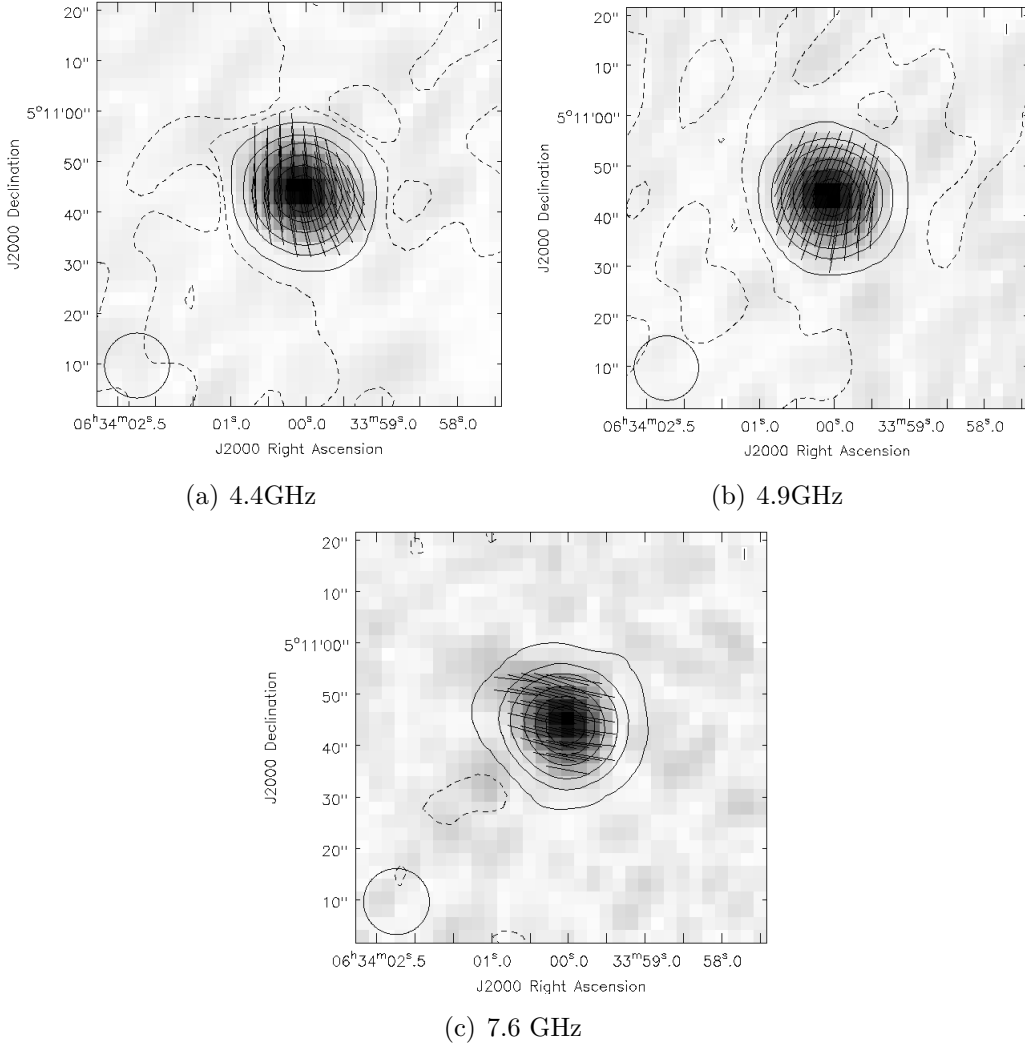


Fig. 2.— Maps of I15 at the three frequencies of observation. The vectors show the polarization position angle, χ , the gray scale is the polarized intensity, L , and the contours are the intensity, I , with contour levels set to -2, -1, 2, 10 20 40 60 and 80% of the peak intensity, which is 19.0 mJy/beam at 4.4GHz. The dashed contours indicate negative intensities, illustrating the level of noise and map imperfections. The circle in the lower left corner indicates the restoring beam.

The fits to the data shown in Figures 4 and 5 are sufficiently good to give us confidence that we have an accurate measure of the RM. Nonetheless, there can be a residual concern that the RM is larger than the value resulting from our fit, and that there is one or more rotations of π radians between the frequencies observed. To exclude this possibility and demonstrate that the 3 frequency RM fits were accurate, we made a $\chi(\lambda^2)$ fit within the

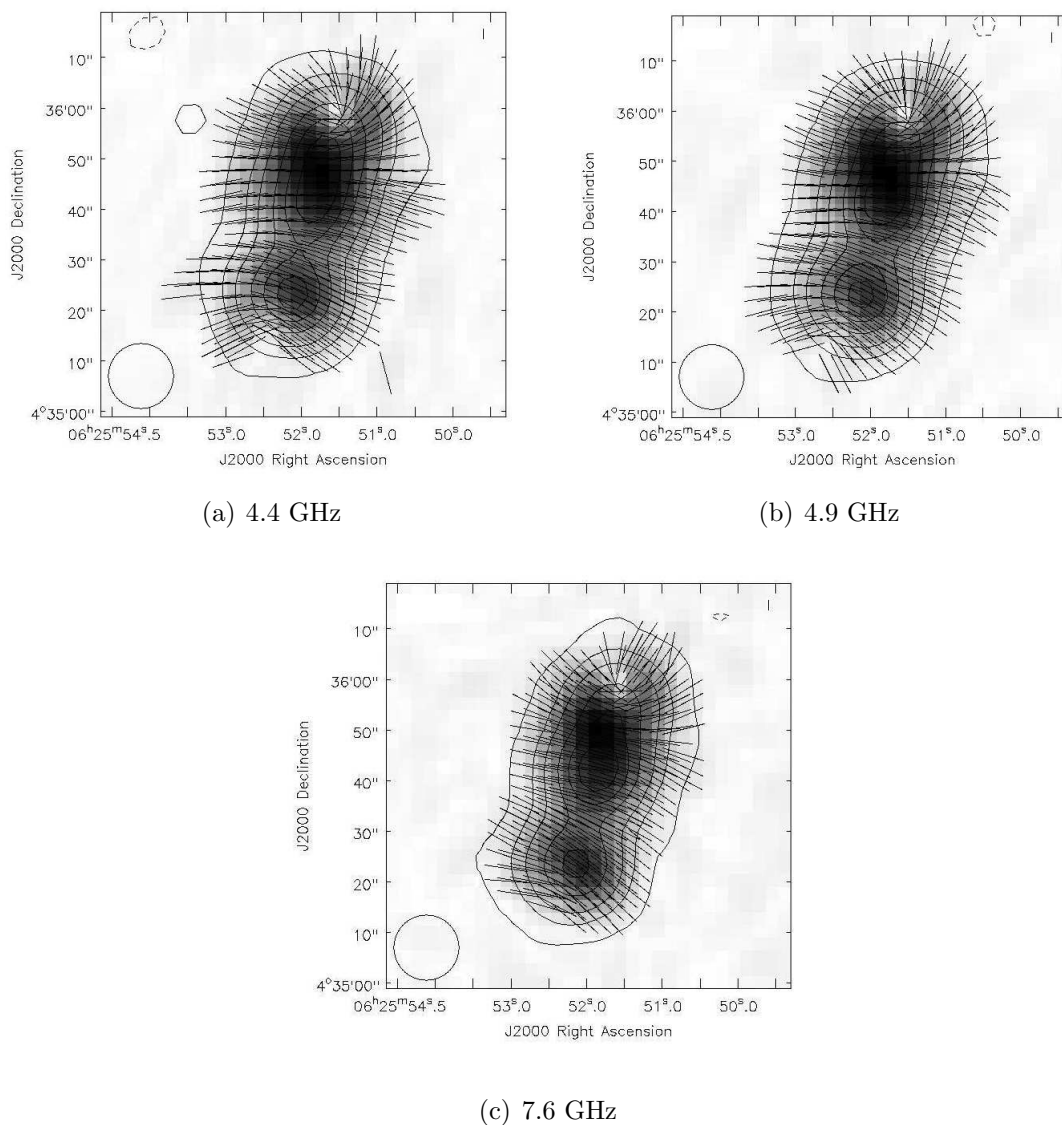


Fig. 3.— Maps of O2 in the same format as Figure 2. The contours of total intensity are at -2, -1, 2, 10, 20, 40, 60 and 80% of the peak intensity, which is 10.2 mJy/beam at 4.4GHz.

4.4GHz bandpass for those sources with $RM \geq 500$ rad m^2 . As described above, the 4.4GHz spectral window had 64 channels of 2MHz bandwidth. The end channels on both ends of the bandpass were discarded, and the remaining channels averaged to 5 sub-IF channels of 22 MHz each. A fit of $\chi(\lambda^2) = \chi_0 + RM\lambda^2$ was then redone over the 4.4GHz spectral window. In all cases, the RM from this procedure agreed, within the errors, with the values obtained by fitting to two or three frequencies of 4.4, 4.9, and 7.6 GHz. A final check of the data set

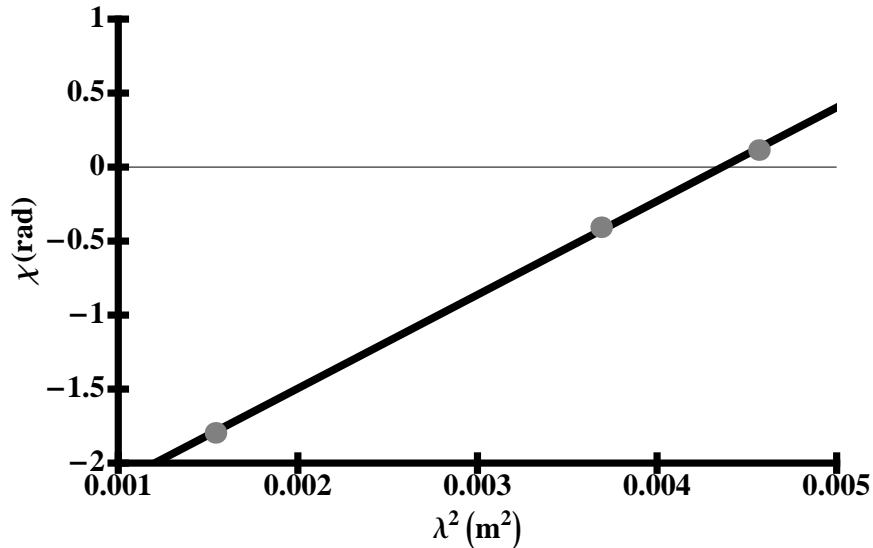


Fig. 4.— A plot of the polarization position angle χ in radians against the square of the wavelength in [m²] for the interior source I15 (Image shown in Figure 2). The value of the fit RM is 633 ± 14 rad m⁻². Error bars are contained within the plotted symbols.

was to examine the degree of linear polarization,

$$m = \frac{L}{I},$$

where I is the total intensity, for each source or source component at each of the frequencies of observation. If the degree of linear polarization is constant, this indicates that the Faraday rotation occurs in an external medium, such as the Galactic interstellar medium. A case where m is a function of frequency, with a smaller m at lower frequencies, indicates internal Faraday rotation and depolarization within the synchrotron emitting source. The dependence of χ on λ is then not proportional to λ^2 , and a fit of the type we have done could yield an inaccurate estimate of the RM.

For each source or source component with measurements at 3 frequencies, the weighted mean degree of linear polarization \bar{m} was calculated from the measurements of m at each of the frequencies. The weighting was with the error on m , calculated from the noise level in the Q and U maps. We then calculated the reduced χ^2_ν statistic for the 3 measurements about this mean (with $\nu = 2$ degrees of freedom), and chose as a flag threshold a value of $\chi^2_\nu = 3.9$, which corresponds to a 2 % probability of constancy of m with frequency, for three measurements (Bevington 1969).

We considered the χ^2_ν statistic as a screening operation rather than a definitive test,

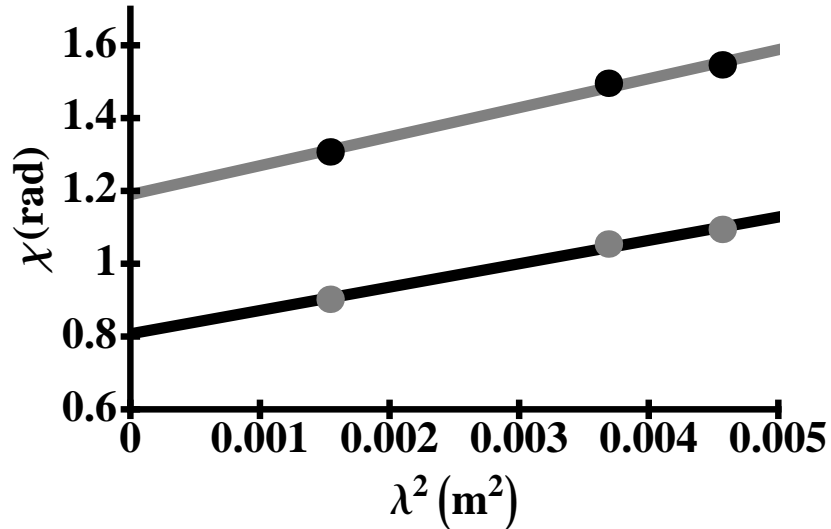


Fig. 5.— Polarization position angle data for source O2, in the same format as Figure 4. The two sets of data points present measurements for the two components of the source seen in Figure 3. The solid black points represent the data for the north component (component (a) in Table 3), and the solid gray points are for the south component (component (b) in Table 3). The fit RM values are $80 \pm 8 \text{ rad m}^{-2}$ for component (a) and $RM= 64 \pm 6 \text{ rad m}^{-2}$ for component (b). Error bars are contained within the plotted symbols.

since the error in m was calculated from the Q and U noise levels on blank portions of the image; such a procedure can underestimate the true error on a portion of the source where L or I is large. Of the 16 sources or source components (excluding I2) with observations at three frequencies, 9 passed this screening operation for m being independent of frequency, and thus unaffected by depolarization.

We then carefully examined the data for the remaining sources in more detail. We found that in nearly every case, depolarization could be excluded, and we concluded that the blank field noise measurements underestimate the true errors in m . For example, for 2 source components (O2a and O5b) the excessive χ_ν^2 was due to m at 7.6 GHz being slightly lower than at 4.4 and 4.9 GHz. This is the opposite of the behavior for Faraday depolarization, and shows that our measurements are not affected by depolarization.

In 4 of the 5 remaining cases, the decrease in m from 7.6 to 4.9 GHz was very small (i.e. $\leq 13 \%$), and we believe the high values of χ_ν^2 are due to the low estimate of measurement errors on m . In all of the aforementioned cases, we feel that a fit of $\chi(\lambda^2)$ gives a good estimate of the RM due to the Galactic ISM, unaffected by the depolarization within the

source. A point in support of this contention is the fact that 3 of these components were in double sources, and the RM s of the two components were in satisfactory agreement (see Table 3, described below).

The only source for which depolarization might be present is I14b. It was flagged by the χ_ν^2 screening criterion, and the degrees of linear polarization at 4.4, 4.9, and 7.6 GHz are 0.018 ± 0.001 , 0.023 ± 0.001 , and 0.031 ± 0.001 , respectively. These measurements seem to show a progression in m with increasing frequency, as well as a reduced χ_ν^2 value formally inconsistent with constancy. These data may indicate depolarization, in which case a source-associated rotation of the position angle, independent of the Galactic ISM, might occur. Furthermore, in this case there is a difference in RM between the two components of the source (see Table 3 below), although a linear fit to the χ versus λ^2 data was obtained. Although this difference in RM between two source components with a small angular separation could indicate a problem with depolarization, it could also be an interesting probe of small scale variations in the nebula, as discussed in Section 4.2 below. In the remainder of this paper, we will use the data for component I14b, with the recognition that the inferred RM might contain a component due to the source itself rather than the Galactic ISM.

A similar test was undertaken, with a corresponding reduction in the degrees of freedom, for the 12 sources or source components with observations at two frequencies. Only 1 source (O7) had a χ_ν^2 for 1 degree of freedom that exceeded the 2 % probability threshold and therefore merited closer examination. We concluded that the large χ_ν^2 was due to small inferred errors on the m values at the 2 frequencies; the m values at 4.4 and 4.9 GHz are in good agreement, with $m_{4.4} > m_{4.9}$. Internal Faraday depolarization or depolarization by a plasma screen in front of the source cannot be occurring in this case.

To conclude, with the probable exception of I2, and the possible but not certain case of I14b, all of the RM values obtained from our sources and source components appear to be measures of the Galactic ISM.

Our results on the polarization properties of our sources and the resultant RM values are shown in Table 3. The first column of Table 3 lists the source name. Duplication of sources in this column indicates that there were two components to the source for which we were able to obtain RM values. Each source has two or three associated rows in the table, and subsequent components of the same source also have two or three rows. These rows give data for the two or three frequencies of observation. Column 2 identifies the components of the duplicated source as either (a) or (b). There were 9 sources that had two components. Column 3 lists the frequency associated with the data for the source, column 4 lists the linear polarized intensity, L (mJy/beam), and the associated error, column 5 the degree of linear polarization, m . Column 6 is the polarization position angle χ and the associated error, and

column 7 has the RM with associated errors. Since the RM is obtained by fitting a line to the $\chi(\lambda^2)$ data for the March and July sources, and by Equation (3) for the August sources, column 7 has one value per source component.

3.3. Comparison of RM Measurements with Taylor et al. (2009)

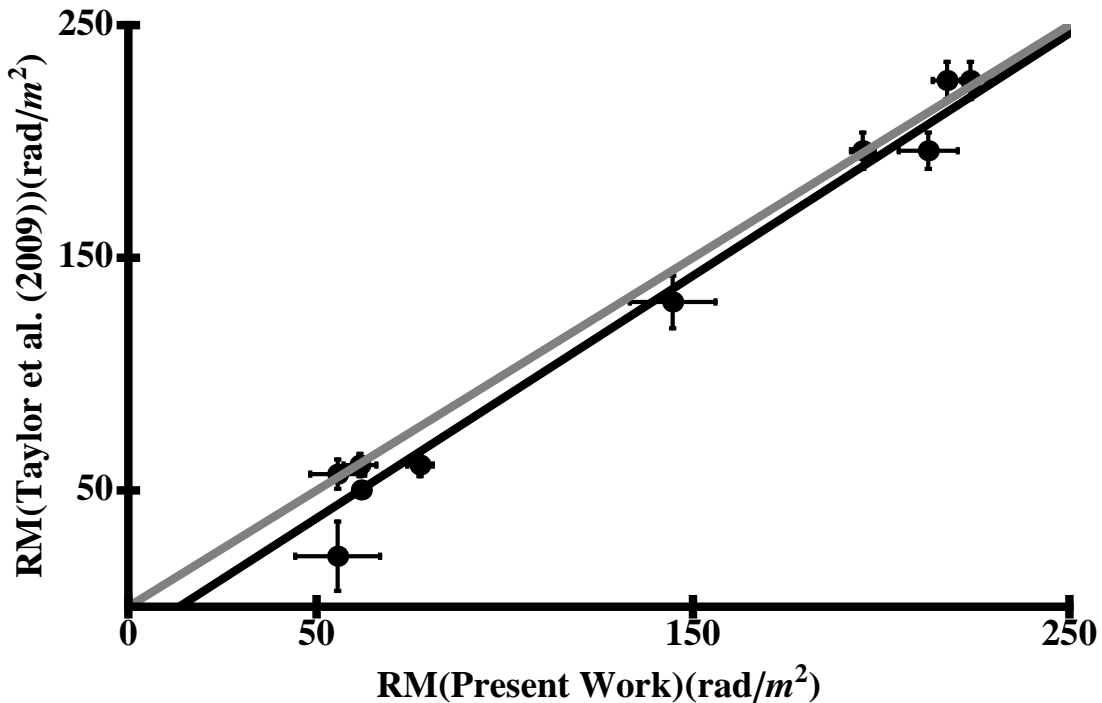


Fig. 6.— A comparison of RM values from Taylor et al. (2009) and the present study. The lighter solid line represents the case of perfect agreement, and the heavy solid line represents a weighted least-squares fit to the data.

Taylor et al. (2009) re-analyzed data from the NRAO VLA Sky Survey (NVSS) in order to obtain RMs for 37,543 radio sources. That study provided RMs for the sky north of -40° in declination. We can compare our RM values with the previously derived RM values by Taylor et al. (2009) for seven of our sources in common with Taylor et al. (2009). There are two reasons for carrying out this comparison. First, it serves as a check on our data and method of data analysis. Second, there are inconsistent reports in the literature regarding the accuracy of the Taylor et al. (2009) results. In a study of the magnetic field in the direction of the Galactic poles, Mao et al. (2010) found discrepancies between their RM measurements and those of Taylor et al. (2009). A comparison of RM values from Taylor et al.

(2009) and independent measurements was also made by Van Eck et al. (2011), with the VLA. Van Eck et al. (2011) found generally satisfactory agreement, although there was a population of outliers as well as an apparent systematic bias at $RM \simeq 50 - 100 \text{ rad m}^{-2}$ (see Figure 4 of Van Eck et al. (2011)). A full discussion of the comparison between independent RM measurements and the RM values from Taylor et al. (2009) is given in Section 4.2 of Harvey-Smith et al. (2011). We think it worthwhile to make additional comparisons between Taylor et al. (2009) and independent measurements made specifically for the purpose of measuring Faraday rotation. Figure 6 illustrates the comparison of our RM measurements with those of Taylor et al. (2009). The sources that are in common are all exterior sources, O1, O2, O4, O7, O9, O15, & O17. None of our interior sources were contained in the catalog of Taylor et al. (2009). Our RM values compare favorably with those of Taylor et al. (2009). The light solid line in Figure 6 shows the case of perfect agreement between the two sets of measurements, and this is clearly a satisfactory representation of the data. A weighted least squares linear fit to the data shown in Figure 6 gives a slope of $m = 1.04 \pm 0.04$ and an intercept of $b = -14.1 \pm 8.1 \text{ rad m}^{-2}$ (heavy solid line). The good agreement between the two sets of measurements is consistent with the assessment of Van Eck et al. (2011), and gives confidence in our RM measurements. We note that this does not address the question of the systematic error in some of Taylor et al. (2009) RM s that was pointed out by Van Eck et al. (2011).

4. Observational Results and Modeling in Terms of the Interaction of an HII Region with the Interstellar Medium

The first question in the analysis is whether the RM data from Table 3 show evidence for an RM enhancement associated with the Rosette Nebula. Such an enhancement is illustrated and clearly seen in Figure 7. In Figure 7, we plot the measured RM versus angular distance from the center of the Rosette Nebula, which we take to be the center of the NGC 2244 star cluster as given by Berghöfer & Christian (2002) (see Introduction). A very clear signature of a Faraday rotation enhancement is seen for the 6 lines of sight (9 sources and source components) with angular separation ≤ 40 arcminutes from the nebular center. The excess RM due to the Rosette Nebula is also visible in Figure 1, in which the size of the plotted symbol for each source is dependent on RM . Those sources viewed through the Rosette have larger RM s. The mean RM for sources seen through the Rosette Nebula is 675 rad m^{-2} , with a range of $200 \leq RM \leq 900 \text{ rad m}^{-2}$. Lines of sight that are more than 40 arcminutes from the center of the nebula have a mean of 147 rad m^{-2} , with a standard deviation of 77 rad m^{-2} . In calculating the mean and standard deviation of the background, we have excluded the two sources in our sample with a negative RM (I18, $RM = -270 \pm 54$

rad m^{-2} & O14(b), $RM = -38 \pm 60$ rad m^{-2}). It is unclear whether the negative RMs have Galactic or extragalactic origins. The RM in both cases was obtained from measurements at only 2 frequencies. As presented in Table 3, both the polarized intensity and degree of linear polarization for those 2 sources are low. Although we include these sources in Table 3 because they passed our selection criteria, we do not include them in our calculation of the Galactic mean background. We interpret this mean background as due to the Galactic Faraday rotation in this part of the sky, which is independent of the Rosette Nebula. The data in Figure 7 show a “RM anomaly” of 50-750 rad m^{-2} associated with the Rosette Nebula. This is comparable to, and perhaps slightly smaller than that reported for the Cygnus OB1 association by Whiting et al. (2009). However, the Whiting et al. (2009) result is more ambiguous because of the angular proximity of other HII regions as well as other Galactic objects, which confuse measurements in that field.

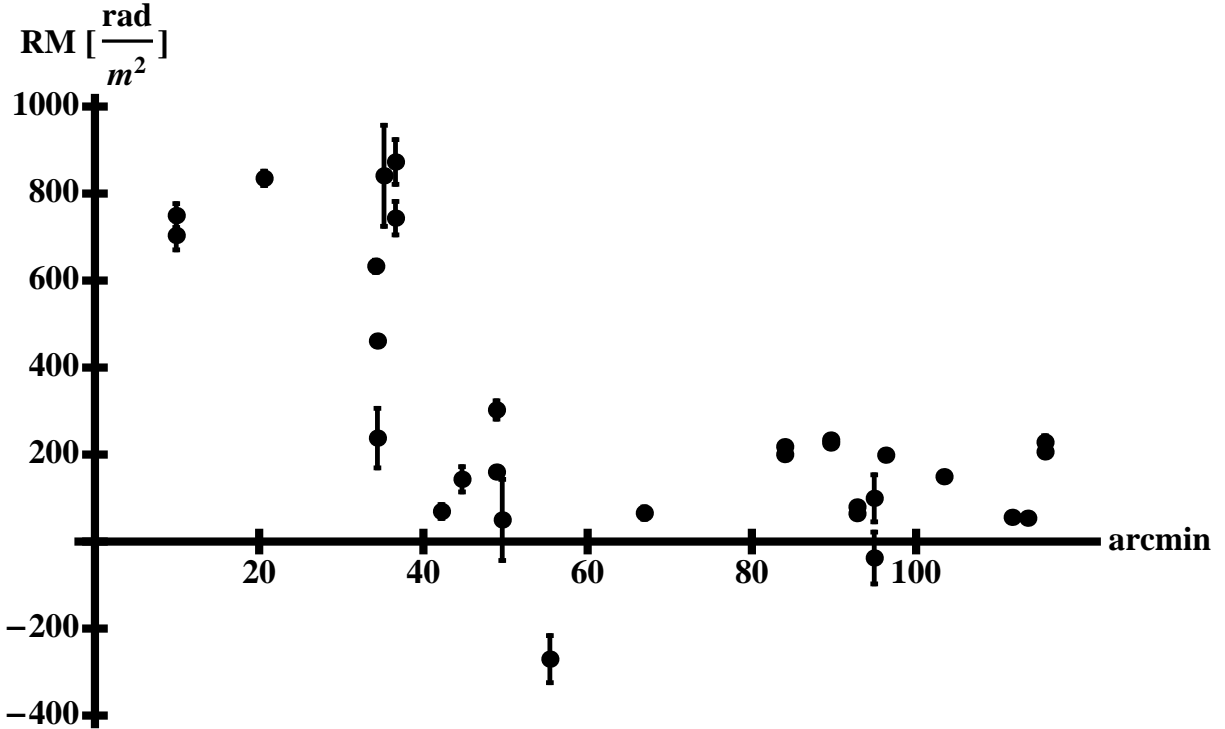


Fig. 7.— The RM (rad m^{-2}) for each source and source component in Table 3 versus angular distance (arcminutes) from the center of the Rosette Nebula. All the sources, and components, are represented on the graph along with the associated error bars.

Table 3. Polarization Results

Source	Component	ν [GHz]	L [mJy/beam]	m [%]	χ [°]	RM [rad m ⁻²]
I1		4.4	0.25 ± 0.03	2	-24.5 ± 3.5	50 ± 93
		4.9	0.26 ± 0.03	3	-27.0 ± 3.4	
I2		4.4	0.15 ± 0.03	0.1	6.8 ± 5	69 ± 16
		4.9	0.37 ± 0.03	0.2	-14.8 ± 1.9	
		7.6	1.70 ± 0.04	1.0	-23.3 ± 0.7	
I6	a	4.4	0.90 ± 0.04	8	13.4 ± 1.1	743 ± 38
	a	4.9	0.78 ± 0.04	7	-23.7 ± 1.7	
I6	b	4.4	0.60 ± 0.03	9	-4.7 ± 1.6	873 ± 51
	b	4.9	0.62 ± 0.03	10	-48.6 ± 2.1	
I7	a	4.4	0.93 ± 0.03	10	-45.4 ± 1.0	749±27
	a	4.9	0.87 ± 0.03	10	-83.1 ± 1.0	
I7	b	4.4	0.79 ± 0.03	5	0.02 ± 1.15	704±33
	b	4.9	0.69 ± 0.03	4	-35.4 ± 1.3	
I8	a	4.4	1.11 ± 0.04	14	46.6 ± 1.0	461±4
	a	4.9	0.99 ± 0.03	13	22.9 ± 0.9	
	a	7.6	0.64 ± 0.04	14	-33.4 ± 1.5	
I8	b	4.4	0.41 ± 0.04	7	28.8 ± 2.6	238± 73
	b	4.9	0.28 ± 0.03	6	6.1 ± 3.2	
	b	7.6	0.21 ± 0.03	7	-13.5 ± 4.7	
I10		4.4	0.23 ± 0.04	2	108.2 ± 5.1	841 ±117
		4.9	0.29 ± 0.03	3	65.9 ± 3.3	
I12		4.4	1.3 ± 0.04	5	61.5 ± 1	835±17
		4.9	1.25 ± 0.04	5	21.9 ± 0.7	
		7.6	1.02 ± 0.05	5	-82.7 ± 1.3	
I14	a	4.4	3.30 ± 0.04	25	59.1 ± 0.3	160 ±3
	a	4.9	2.96 ± 0.03	26	51.4 ± 0.3	
	a	7.6	1.78 ± 0.04	25	31.4 ± 0.6	
I14	b	4.4	0.75 ± 0.04	2	106.4 ± 1.3	303±21
	b	4.9	0.90 ± 0.03	2	87.4 ± 1.0	
	b	7.6	0.86 ± 0.04	3	53.0 ± 1.3	
I15		4.4	0.93 ± 0.04	5	6.6 ± 1.1	633±14

Table 3—Continued

Source	Component	ν [GHz]	L [mJy/beam]	m [%]	χ [°]	RM [rad m ⁻²]
		4.9	0.89 ± 0.04	5	-23.3 ± 1.2	
		7.6	0.56 ± 0.04	4	-102.9 ± 1.9	
I16		4.4	0.94 ± 0.03	11	84.2 ± 1.0	143±29
		4.9	0.81 ± 0.03	10	77.0 ± 1.1	
I18		4.4	0.45 ± 0.03	4	28.2 ± 1.6	-270±54
		4.9	0.38 ± 0.03	4	41.8 ± 2.3	
O1		4.4	5.75 ± 0.05	6	-55.5 ± 0.2	54±7
		4.9	5.09 ± 0.06	6	-58.2 ± 0.3	
O2	a	4.4	4.89 ± 0.05	5	88.6 ± 0.3	80±8
	a	4.9	4.42 ± 0.04	5	85.7 ± 0.3	
	a	7.6	3.16 ± 0.06	4	74.9 ± 0.5	
O2	b	4.4	3.43 ± 0.05	4	62.7 ± 0.4	64±6
	b	4.9	3.20 ± 0.05	4	60.4 ± 0.5	
	b	7.6	2.59 ± 0.06	4	51.7 ± 0.7	
O4	a	4.4	4.28 ± 0.04	23	49.7 ± 0.3	200±1
	a	4.9	3.92 ± 0.04	23	39.5 ± 0.3	
	a	7.6	2.69 ± 0.04	23	15.0 ± 0.5	
O4	b	4.4	1.60 ± 0.05	6	-9.4 ± 0.8	218 ±8
	b	4.9	1.45 ± 0.05	6	-19.1 ± 0.8	
	b	7.6	1.10 ± 0.04	6	-47.0 ± 1.1	
O5	a	4.4	1.24 ± 0.05	11	85.8 ± 1.1	206±10
	a	4.9	1.05 ± 0.05	11	74.0 ± 1.3	
	b	7.6	0.73 ± 0.04	11	49.9 ± 1.8	
O5	b	4.4	1.07 ± 0.05	4	79.0 ± 1.3	228±15
	b	4.9	0.96 ± 0.05	4	69.6 ± 1.4	
	b	7.6	0.54 ± 0.04	3	39.6 ± 2.5	
O7		4.4	4.03 ± 0.05	2	19.3 ± 0.4	55±11
		4.9	3.84 ± 0.06	2	16.5 ± 0.4	
O9	a	4.4	4.00 ± 0.04	14	93.5 ± 0.3	226±1
	a	4.9	3.69 ± 0.05	14	81.9 ± 0.4	
	a	7.6	2.42 ± 0.05	14	54.2 ± 0.6	

4.1. Comparison of Observations to HII Region Shell Models

In this section, we compare our observations with mathematically simple expressions which describe the dynamics of an HII region interaction with the surrounding ISM. The first is the model presented in Whiting et al. (2009). The Whiting et al. (2009) model contains a simple parameterization of a stellar bubble, as described by the theory of Weaver et al. (1977). In that model, the HII region consists of an inner, low density cavity comprised of shocked stellar wind, and a contact discontinuity (assumed spherical) separating the shocked stellar wind from interstellar medium material. This interstellar medium material is shocked and photoionized interstellar gas which has passed through an outer shock. The last part of the bubble structure is the outer shock itself.⁴ The parameters of the model are R_0 , the outer radius of the shell; R_1 , the inner radius of the shell; n_e , the plasma density within the shell ($n_e=0$ is assumed for $r < R_1$); and \vec{B}_0 , the interstellar magnetic field outside the shell. A distinction is made between the pristine magnetic field \vec{B}_0 upstream of the outer shock, and the downstream magnetic field inside the plasma shell, which has been modified by passage through the shock.

Whiting et al. (2009) obtain the following formula for the RM through such a shell.

$$RM(\xi) = \frac{Cn_eL(\xi)}{2} [B_{ZI} + B_{ZE}] \quad (6)$$

where n_e is the plasma density (electron density) in the shell, $L(\xi)$ is the length of the chord through the shell, and B_{ZI} and B_{ZE} are the downstream line of sight components of the magnetic field at the points where the line of sight enters (ingress) and leaves (egress) the shell respectively, given in Equations (7) - (9) of Whiting et al. (2009). The variable ξ is the transverse, linear distance between the line of sight and a line of sight passing through the center of the shell (i.e., $\xi=0$ is a line of sight through the center of the shell and $\xi=R_0$ is a line of sight which is tangent to the outer edge of the shell.). The constant C is the collection of fundamental physical constants in curved brackets in Equation (1). The constant C has the value 2.631×10^{-17} in cgs units, or 0.81 if “interstellar units” of cm^{-3} , μGauss , and parsecs are chosen for n_e , \vec{B}_0 , and L , respectively. $L(\xi)$ is given by

$$L(\xi) = 2R_0\sqrt{(1 - (\xi/R_0)^2)}, \text{ if } \xi \geq R_1 \quad (7)$$

$$L(\xi) = 2R_0[\sqrt{(1 - (\xi/R_0)^2)} - (R_1/R_0)\sqrt{(1 - (\xi/R_1)^2)}], \text{ if } \xi \leq R_1$$

⁴This model is described in more detail in Section 5.1 of Whiting et al. (2009), and illustrated in Figure 6 of that paper.

Table 3—Continued

Source	Component	ν [GHz]	L [mJy/beam]	m [%]	χ [°]	RM [rad m ⁻²]
O9	b	4.4	2.93 ± 0.04	9	83.0 ± 0.4	
	b	4.9	2.76 ± 0.05	10	71.0 ± 0.5	233±1
	b	7.6	1.82 ± 0.05	10	42.5 ± 0.8	
O14	a	4.4	0.55 ± 0.04	9	-81.3 ± 2.0	
	a	4.9	0.51 ± 0.04	9	-86.3 ± 2.0	99±54
O14	b	4.4	0.49 ± 0.04	9	9.7 ± 2.15	
	b	4.9	0.46 ± 0.04	9	11.6 ± 2.2	-38±60
O15		4.4	22.67 ± 0.06	8	18.3 ± 0.1	
		4.9	20.80 ± 0.06	8	16.4 ± 0.1	65±14
		7.6	14.87 ± 0.11	8	6.6 ± 0.2	
O16		4.4	3.23 ± 0.05	13	-70.8 ± 0.4	
		4.9	2.96 ± 0.04	13	-81.6 ± 0.4	199±6
		7.6	1.94 ± 0.05	13	-105.3 ± 0.7	
O17		4.4	2.52 ± 0.03	10	-27.2 ± 0.4	
		4.9	2.28 ± 0.03	10	-34.7 ± 0.4	149±11

Exterior to the shell, we assume the magnetic field of the interstellar medium is uniform, but it will be modified in the shell. The theory of magnetohydrodynamic shock waves (e.g. Gurnett & Bhattacharjee (2005)) shows that the magnetic field component in the shock plane is amplified by a factor X , and the component normal to the shock front is unchanged. The factor X , for the case of a strong shock, is equivalent to the density compression ratio. We redefine the B_{ZI} and B_{ZE} components in terms of B_{0Z} , the upstream line of sight component of the magnetic field. Employing these assumptions and definitions in Equation (6), we have

$$RM(\xi) = Cn_eL(\xi)B_{0Z} \left[1 + (X - 1) \left(\frac{\xi}{R_0} \right)^2 \right] \quad (8)$$

It should be pointed out that our shell model, expressed in Equations (6)-(8), assumes that the post-shock field strength at the ingress or egress point applies everywhere along the half-chord connecting the ingress or egress point to the midpoint of the chord (see Figure 6 of Whiting et al. (2009) for an illustration). No attempt is made here to confront the physically complex question of the shell magnetic field as a function of position throughout the shell. Our approximation is presumably accurate for a thin shell, in which the chord extends only a short distance from the shock front before entering the bubble interior (again, see Figure 6 of Whiting et al. (2009)). However, in the case of a thick shell, this approximation must break down, and Equation (8) must be inaccurate. Other than recognizing this fact, further investigation is beyond the scope of this paper. This recognition should motivate further theoretical work to obtain analytic expressions which incorporate the results of MHD calculations such as Ferrière et al (1991) and Stil et al. (2009). For our model of Equation (8), we adopt the shell parameters from Celnik (1985), where $R_0 = 16.9$ parsecs, $R_1 = 6.2$ parsecs, and $n_e = 10.8 - 15.5 \text{ cm}^{-3}$. These numbers refer to Celnik’s Model 1, which is the single shell model. For the calculations described below we utilize a density equal to the mean of Celnik’s values, $n_e = 13.1 \text{ cm}^{-3}$. The variable B_{0Z} , the z component of the upstream ISM magnetic field, is

$$B_{0Z} = B_0 \cos \theta,$$

where B_0 is the magnitude of the general interstellar field. In the analysis of this paper, we assume B_0 to be a known constant, and θ to be a variable with a wide range of possible values at a given point in the Galaxy. The justification for this choice is the rather well established value for the magnitude of the magnetic field in the low density phases of the ISM (e.g. Ferrière 2011; Crutcher et al 2010). We choose $B_0 = 4 \mu\text{G}$ in the calculations below. The angle θ may have a well-defined expectation value for the location of the Rosette Nebula in the Galaxy, but the actual value at a specific location and time presumably departs significantly from this expectation value due to turbulent fluctuations in the ISM. A meaningful analogy would be the interplanetary magnetic field at 1 AU. Although the average direction conforms

to the Parker spiral, a measurement at a given time shows the field pointing in a wide range of directions.

It should be recognized that in reality, both B_0 and θ are random variables with mean values and probability density functions. As such, the true unknown variable is B_{0z} which is formed from them. Again, observations of the solar wind prove instructive. Examination of several days of interplanetary magnetic field measurements show that the angles defining the direction of the interplanetary field show random variations, but the magnitude of the field does as well. The solar wind provides some support for our practice in the present case. Although the magnitude of the field does change with time, the fractional changes are usually relatively small in comparison with the large variations in the orientation of the interplanetary field. This statement is supported by the well known observational result that the variance of the magnitude of the interplanetary field is much less than the variance in the components (Bruno and Carbone 2005).

In comparing the model of Equation (8) with our data, we overlaid curves generated by Equation (8) on a plot of the RM vs the distance ξ in parsecs from the center of the Rosette (Figure 8), and effectively used the free parameter θ as a “tuning knob” for the model. By doing so, we obtained a value of $\theta = 72^\circ$ such that the model reproduces the magnitude of the measured RMs, and their dependence on the distance from the center of the Rosette Nebula. The degree of agreement between the model and the data in Figure 8 is actually quite good, particularly since we have adopted the shell model parameters R_0 , R_1 , and n_e directly from the data of Celnik (1985). We have not varied these parameters in an attempt to optimize the fit. Figure 9 presents the shell model with altered radii in order to obtain a better fit for the model Equation (8) to the data.

To fit the magnitudes of the RMs viewed through the nebula, our model requires that the interstellar magnetic field at the location of the Rosette Nebula (before modification by the bubble associated with the Rosette) be rather highly inclined to the line of sight. Interestingly, our value of θ is roughly consistent with that expected for the mean Galactic field at the location of the Rosette Nebula. We use the galactic longitude of 206.5° for the Rosette, and assume a Galactocentric distance of the Sun of 8.5 kpc, and a distance to the Rosette of 1.6 kpc. In this case, the angle between the line of sight and an azimuthal magnetic field is 68° . This is obviously completely consistent (to a doubtlessly fortuitous degree) with our model value of $\theta = 72^\circ$.

Studies of the functional form of the Galactic magnetic field, while not conclusive at discriminating between an azimuthal field and one which follows the spiral arms, indicate that the field in the approximate neighborhood of the Sun has a pitch angle of -8° (Beck 2001; Ferrière 2011). Application of this pitch angle to an azimuthal field would then

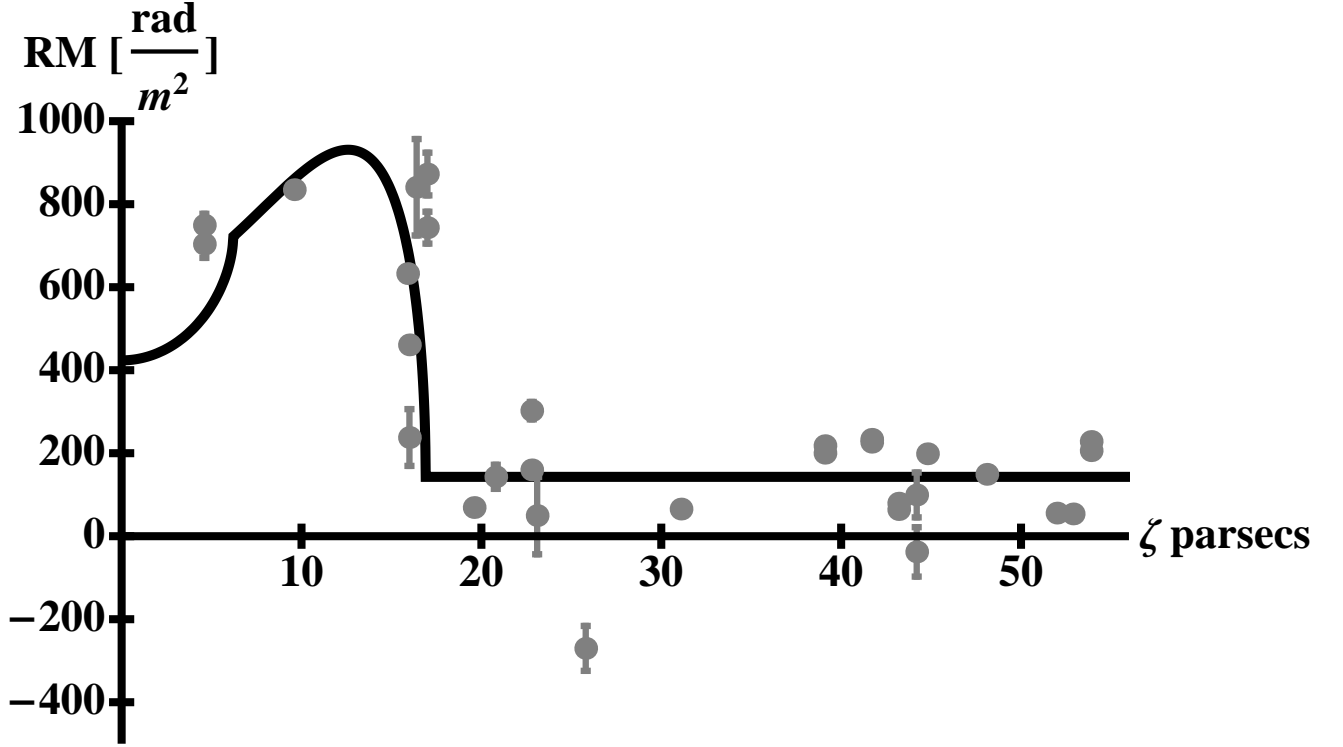


Fig. 8.— Plot of RM versus distance from center of the Rosette Nebula. This plot differs from Figure 7 in that the distance of the lines of sight from the nebular center have been converted from arcminutes to parsecs, and the model for Faraday rotation through a stellar bubble given by Equation (8), has been overplotted. This model utilizes the following shell parameters: $R_1=6.2$ pc, $R_0=16.9$ pc, and $n_e=13.1$ cm^{-3} . Achieving this fit requires that the interstellar magnetic field at the location of the Rosette Nebula has a magnitude of 4 μG and is inclined at an angle $\theta=72^\circ$ with respect to our line of sight.

produce an expected angle of 60° between the mean Galactic field at the location of the Rosette and the line of sight. This value is also in acceptable agreement with our inferred value, in that it indicates a magnetic field that is oriented at a large angle with respect to the line of sight.

We now consider a quite different HII region model which has been discussed in the context of Faraday rotation “anomalies”, that of Harvey-Smith et al. (2011) discussed in Section 1.3 above. Harvey-Smith et al. (2011) concluded that the magnetic field was not amplified in the volume of the HII region. We have adjusted our Equation (6) to express the Harvey-Smith et al. (2011) assumption of no \vec{B} field amplification, giving the formula

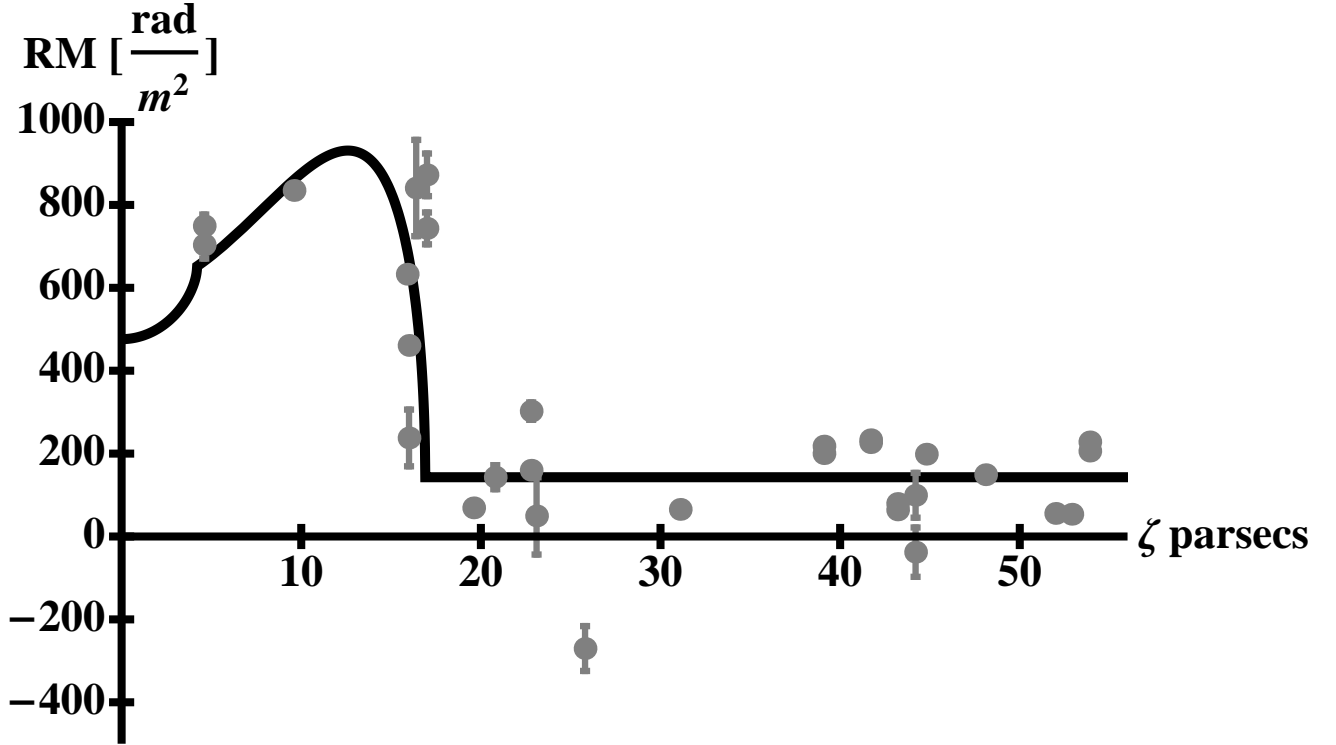


Fig. 9.— This plot is the same as Figure 8 except the inner radius of the shell has been changed to optimize the fit to the data, $R_1=4.2$ pc. The value of θ is $\theta = 72^\circ$.

$$RM(\xi) = Cn_e L(\xi) B_{0Z} \quad (9)$$

where all parameters are defined following Equation (6). The difference between these two expressions is that Equation (9) does not include amplification of the “upstream” interstellar magnetic field by the outer shock of the stellar bubble. As before, θ is the only free parameter and was varied to obtain a fit to the observed RM observations. By visual inspection, we obtained $\theta=54^\circ$ for reasonable agreement between Equation (9) and the data. A comparison of the model given by Equation (9) with the data is shown in Figure 10. Although it produces the magnitude and angular scale of the RM anomaly, it arguably does not do as well in reproducing the observed dependence of RM on distance from the center of the nebula. The smaller inclination of the interstellar magnetic field ($\theta=54^\circ$) is easily understood since in this latter model, there is no amplification of the perpendicular component of the interstellar magnetic field at the outer shock front (see Equation 9 of Whiting et al. (2009)). We suggest that the model of Whiting et al. (2009) provides a better fit to the observed dependence of RM on distance from the center of the nebula for the case of the Rosette

Nebula. To distinguish between these two models will require more lines of sight which pass between the inner and outer radii of the bubble (6 and 17 parsecs in the case of the Rosette Nebula). For the shell models described by Equation (9), in which the pre-existing interstellar magnetic field is unaltered by the presence of the HII region, the RM should have a maximum near the inner radius, as shown in Figure 10. In the model of Whiting et al. (2009), on the other hand, the magnetic field is amplified and “refracted” into the shock plane. This has the potential of producing “RM limb brightening”, as might be present in the Rosette Nebula data, Figures 8 and 9. This situation might be clarified by RM measurements of an additional 11 sources that were made with the VLA in February 2012, and are currently awaiting reduction and analysis.

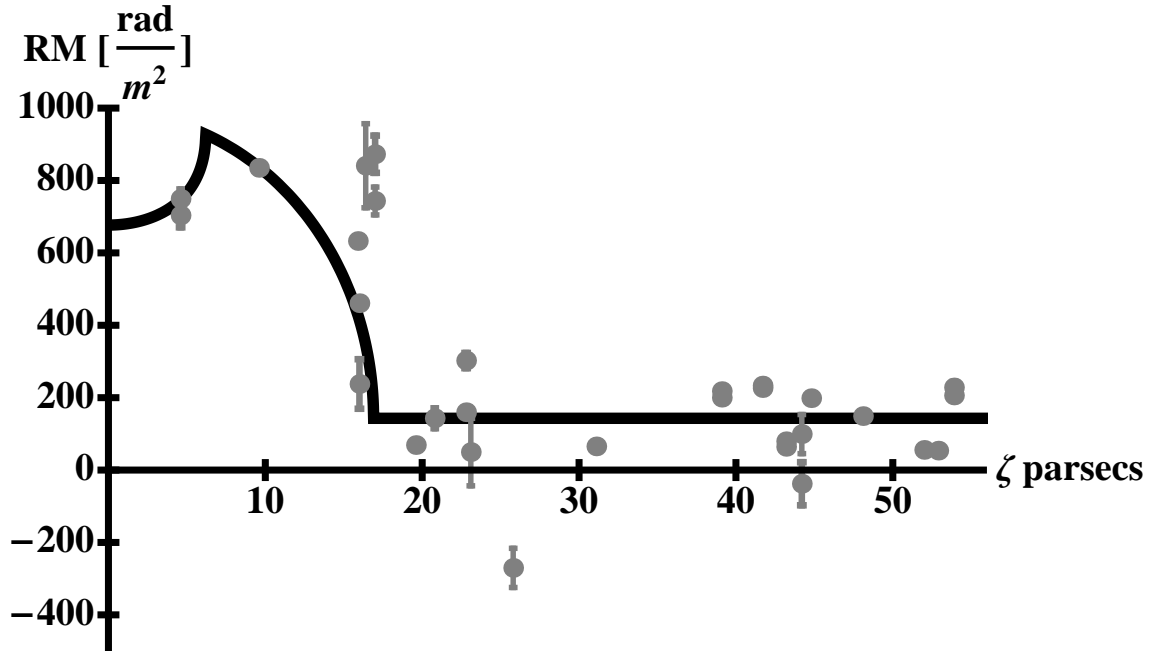


Fig. 10.— This plot is the same as Figures 8 and 9 except the model that has been overplotted is given by Equation (9) (interstellar magnetic field unmodified by HII region). This model curve requires that the interstellar magnetic field at the location of the Rosette Nebula is inclined at an angle $\theta=54^\circ$ with respect to our line of sight.

The fit value for θ probably does not have much diagnostic ability, at least in the case of a single nebula. The values of θ for an azimuthal Galactic magnetic field (68°), or a spiral field with a pitch angle of -8° , $\theta = 60^\circ$ are more or less equally compatible with our shell model or the unmodified field model, Equation (9). However, all studies of the Galactic magnetic field show that the random component of the field is comparable to, if not larger than, the mean systematic component (e.g. Rand and Kulkarni 1989; Minter & Spangler

1996; Haverkorn et al. 2006). Thus the interstellar magnetic field at the location of the Rosette is doubtlessly comprised of a mean, large scale component which is inclined at a large angle to the line of sight, and a random, turbulent component which is isotropic. As a result, the “local” interstellar magnetic field at the Rosette Nebula could point in virtually any direction.

There are some final and obvious remarks which should be made regarding a comparison between the results of the present study of the Rosette Nebula and those of Harvey-Smith et al. (2011) on 5 other HII regions. The model of Whiting et al. (2009) assumes that the plasma shell around the HII region is a bubble as described by the theory of Weaver et al. (1977). The formation of a bubble on the scale of the Rosette Nebula requires stars with very large wind luminosities, which can only be furnished by very early main sequence stars or Wolf-Rayet stars. Such stars will only be found in very young stellar associations. At a later time, stellar wind luminosities will subside and the wind-blown bubble or superbubble will cease to exist. As was discussed in the Introduction, the Rosette Nebula is an excellent candidate for a stellar superbubble. The observations of Menon (1962) showed that it has the annular shell structure expected of such a bubble, and it has been used as a paradigmatic wind-blown structure in theoretical studies [e.g. Dorland et al. (1986); Dorland & Montmerle (1987)]. It therefore would be expected, *a priori*, to show the plasma structure expected for a bubble.

The HII regions studied by Harvey-Smith et al. (2011) could well be older clusters that are past the age when luminous stellar winds dominate their surroundings in the ISM. Resolution of this interesting question will require further observations of a sample of HII regions, with independent information on the ages of the star clusters and the wind luminosities of the constituent stars.

4.2. Differences in Rotation Measure Between Closely-Spaced Lines of Sight

The data in Table 3 show several cases in which RM is measurable for two components within the same source. This raises the possibility of measuring RM differences between closely-spaced lines of sight. Spangler (2007) uses the term *differential Faraday rotation* to describe such differences. In the case of the present observations, with a synthesized beam width (FWHM) of 12''8 and an assumed distance to the Rosette Nebula of 1600 pc, we can examine lines of sight separated by as little as 0.1 parsecs.

Differential Faraday rotation observations have been discussed by many authors (e.g. Minter & Spangler 1996; Haverkorn et al. 2008). Measurements of the RM difference ΔRM on many pairs of lines of sight with a range of angular separations $\delta\theta$ can be used to construct

the RM structure function $D_{RM}(\delta\theta)$. The RM structure function yields characteristics of interstellar plasma turbulence (Minter & Spangler 1996; Haverkorn et al. 2008). Spangler (2007) also pointed out that a measurement of differential Faraday rotation could indicate the presence of an electrical current flowing between the lines of sight, and used a measurement of differential coronal Faraday rotation to deduce a model-dependent value for the magnitude of coronal currents. The same ideas could be applied to measurements of interstellar Faraday rotation.

In this subsection, we briefly discuss the status of differential Faraday rotation in our sample of sources. Nine of the sources in Table 3 have RM values for two source components. We restrict attention to those sources with χ measurements at three frequencies. Such observations provide more secure and precise RM values. These sources are I8, I14, O2, O4, O5, and O9. Obviously, with such a restricted set of data we cannot construct a RM structure function, and our comments here will remain qualitative.

We first consider the four “exterior” sources O2, O4, O5, and O9. The RM values for these sources are presumably determined by the general interstellar medium, with no contribution from the Rosette Nebula. The ΔRM values for these sources range from $\sim 7 - 25 \text{ rad m}^{-2}$, and in at least 2 cases (O5 and O9) seem consistent with zero, given the measurement errors. The other two exterior sources (O2 and O4) have ΔRM values which appear slightly larger than expected for noise fluctuations about a zero expectation value.

The two “interior” sources I8 and I14 have ΔRM values in excess of 100 rad m^{-2} , and larger than expected from our error estimates. This would seem to indicate enhanced differential Faraday rotation for lines of sight that pass through the interior of the Rosette Nebula, implying higher levels of plasma turbulence or electrical current systems flowing in the bubble associated with the Rosette. However, two caveats should be noted. First, as noted in Section 2, it is possible that component b of I14 is internally depolarized at the frequencies of observation, in which case neither the fit RM for component b nor the measured ΔRM between the two components is a diagnostic of the ISM. Second, the small number of sources we are considering (2 interior and 4 exterior sources) precludes any firm conclusions about the statistics of differential Faraday rotation inside and outside of the Rosette Nebula.

Given the data available in the present paper, a possible enhancement in ΔRM for the interior source I8 (and perhaps I14) relative to the exterior sources is speculative. The statistics of differential Faraday rotation for lines of sight passing through the Rosette Nebula, and the comparison with the statistics for lines of sight which do not pass through the nebula, need to be determined by measurements for a larger number of sources. As mentioned in Section 4.1, multifrequency polarization measurements of an additional 11 sources with lines

of sight through the nebula have been made and are awaiting reduction and analysis. Those data should determine if an enhancement in differential Faraday rotation due to the Rosette Nebula exists, and if it does exist, establish its properties.

5. Summary and Conclusions

The conclusions of this paper are as follows.

1. We observed 23 extragalactic radio sources whose lines of sight pass through or close to the Rosette Nebula and obtained Faraday rotation measurements for 21 of them. The interior sources, whose lines of sight pass through the Rosette, have an excess RM of 50-750 rad m⁻² with respect to a background due to this part of the galactic plane, which we determined to be +147 rad m⁻². We interpret this 50-750 rad m⁻² excess as the Faraday rotation measure of the plasma shell which comprises the Rosette Nebula.
2. We have compared our observations with a simplified analytic model for the plasma shell associated with a wind-driven, photoionized stellar bubble surrounding the NGC 2244 star cluster. This model was derived and presented in Whiting et al. (2009). We find the measurements adhere well to the model if the angle between the line of sight and the Galactic magnetic field at the location of the Rosette Nebula is $\theta=72^\circ$ (see Figure 8). This angle is compatible with that expected for the mean Galactic field at the location of the Rosette Nebula ($60^\circ - 68^\circ$). Our observations support an interpretation in which the Rosette Nebula is a wind-blown bubble as described by the theory of Weaver et al. (1977).
3. We have also compared our observations with a simpler model in which the NGC 2244 star cluster photoionizes the surrounding gas without modifying the magnetic field, as proposed by Harvey-Smith et al. (2011). This model, unlike the stellar bubble model, does not naturally account for the observed, annular shell structure of the Rosette Nebula. This model can also reproduce the magnitude of the RMs measured through the Rosette Nebula, with a smaller angle between the line of sight and the interstellar field at the location of the Rosette ($\theta=54^\circ$). This model does not seem to account as well for the observed dependence of RM on the projected distance from the center of the nebula.
4. A determination of which of these models, if either, is better for the plasma structure of HII regions will require similar studies of more HII regions (with large numbers of lines of sight per HII region), spanning a range in age of the embedded star clusters.

5. We have compared our *RM* values with those of Taylor et al. (2009) for the 7 sources (with 10 source components) in common. Good agreement between the two sets of measurements was found. This comparison was principally undertaken as a check of the *RMs* resulting from our observations, but it also contributes to the literature on the accuracy of the large Taylor et al. (2009) *RM* data set. Our limited investigation supports the general accuracy of the Taylor et al. (2009) data, but does not contradict the finding of episodic inaccuracies or biases, as discussed in Van Eck et al. (2011).

This research was supported at the University of Iowa by grant AST09-07911 and ATM09-56901 from the National Science Foundation. We are also grateful for advice and assistance from the staff of the National Radio Astronomy Observatory, Socorro, New Mexico. We thank the referee of this paper for a helpful and collegial review. We also thank Professors Marijke Haverkorn of Radboud University, Nijmegen, and Katia Ferrière of the University of Toulouse for insightful, interesting, and helpful reviews of this paper.

REFERENCES

- Beck, R. 2001, *Space Sci. Rev.* 99, 243
- Berghöfer, T. W. & Christian, D. J. 2002, *A&A* 384, 890
- Bevington, P.R., *Data Reduction and Error Analysis for the Physical Sciences*, McGraw-Hill: New York
- Bignell, C., Polarimetry, in *Synthesis Mapping. Proceedings of the NRAO-VLA Workshop*, entitled by A. R. Thomspon and L. R. D’Addario, 6, 1982, 6-1-6-29
- Brown, J. C., Taylor, A. R., and Jackel, B. J. 2003, *ApJS* 145, 213
- Brown, J. C., Haverkorn, M., Gaensler, B. M., et al. 2007, *ApJ* 663, 258
- Bruno, R. & Carbone, V. 2005, *Living Rev. Sol. Phys.* 2, 4
- Celnik, W. E. 1983, *A&AS* 53 403
- Celnik, W. E. 1985, *A&A* 144,171
- Condon, J. J., Cotton, W. D., Greisen, E. W., et al. 1998, *AJ* 115 1693
- Crutcher, R.M., Wandelt, B., Heiles, C., Falgarone, E., & Troland, T.H. 2010, *ApJ* 725, 466

- Dorland, H., Montmerle, T., & Doom, C. 1986, A&A 160, 1
- Dorland, H. & Montmerle, T. 1987, A&A 177, 243
- Ferrière, K., MacLow, M.M., & Zweibel, E.G. 1991, ApJ 375, 239
- Ferrière, K. 2011, Mem. Soc. Astr. It. 82, 824
- Freyer, T., Hensler, G., and Yorke, H. W. 2003, ApJ 594, 888
- Gurnett, D. A. & Bhattacharjee, A. 2005, Introduction to Plasma Physics (Cambridge: Cambridge Univ. Press)
- Haffner, L. M., Reynolds, R. J., Tufte, S. L., et al. 2003, ApJS 149, 405
- Harvey-Smith, L., Madsen, G. J., & Gaensler, B. M. 2011, ApJ 736, 83
- Haverkorn, M., Gaensler, B. M., McClure-Griffiths, N. M., Dickey, J. M., & Green, A. J. 2004, ApJ 609, 776
- Haverkorn, M., Gaensler, B. M., Brown, J. C., et al. 2006, ApJ 637, L33
- Haverkorn, M., Brown, J.C., Gaensler, B.M., and McClure-Griffiths, N.M. 2008, ApJ 680, 362
- Ingleby, L. D., Spangler, S. R., & Whiting, C. A. 2007, ApJ 668 520I
- Lazio, T. J., Spangler, S. R., & Cordes, J. M. 1990, ApJ 363, 515
- Mancuso, S. and Spangler, S. R. 2000, ApJ 539, 480M
- Mao, S. A., Gaensler, B. M., Haverkorn, M., et al. 2010, ApJ 714, 1170
- Menon, T. K.1962, ApJ 135, 394
- Minter, A. H. & Spangler, S. R. 1996, ApJ 458, 194
- Ogura, K. & Ishida, K. 1981, PASJ 33, 149
- Digitized Sky Survey, Association of Universities for Research in Astronomy, Inc. 1994 *http://stdu.stsci.edu/cgi-bin/dssform*
- Park, B. & Sung, H. 2002, AJ 123, 892
- Pérez, M. R., Joner, M. D., Thé, P. S., & Westerlund, B. E. 1989, PASA 101, 195

- Rand, R.J. & Kulkarni, S.R. 1989, ApJ 343, 760
- Román-Zúñiga, C. G. & Lada, E. A. 2008, in “Handbook of Star Forming Regions Vol. I: The Northern Sky”, Astron. Soc. Pac. Monograph Publications vol. 4, ed: Bo Reipurth
- Sakurai, T. & Spangler, S. R. 1994, Radio Science 29, 635
- Spangler, S.R. 2007, ApJ 670, 841
- Spitzer, L. 1968, Diffuse Matter in Space, Wiley Interscience.
- Stil, J., Wityk, N., Ouyed, R., & Taylor, A. R. 2009, ApJ 701, 330
- Taylor, A. R., Stil, J. M., & Sunstrum, C. 2009, ApJ 702, 1230
- Vallee, J. P. 1993, ApJ 419, 670
- Vallee, J. P. 2004 New A Rev., 48, 763
- Van Eck, C. J., Brown, J. C., Stil, J. M., et al. 2011, ApJ 728,97
- Wang, J., Townsley, L. K., Feigelson, E. D., et al. 2008, ApJ 675, 464
- Weaver, R., McCray, R., Castor, I., Shapiro, P., & Moore, R. 1977, ApJ 218, 377
- Whiting, C. A., Spangler, S. R., Ingleby, L. D., & Haffner, M. L. 2009, ApJ 694, 1452